Effects of transfer processes on the marine atmospheric boundary layer

Ann-Sofi Smedman, Ulf Högström and Erik Sahlee

Department of Earth Sciences, Meteorology,Uppsala University,
Uppsala, Sweden

1.   Introduction

Oceans occupy more than 70% of the Earth surface. Correct parameterization of the exchange of momentum and heat is crucial for climate modelling and weather forecasts. In models the coupling between the lowest model level and the surface is described through the Monin-Obukhov similarity theory, a theory which is well tested over land. But is it also valid over the sea? Two striking differences between land and sea are the increase of roughness length (waves) with wind speed and the large heat capacity in the ocean leading to small diurnal variation.

This presentation will deal with i) the influence of waves on the turbulence structure in the marine atmospheric boundary layer (MABL) and ii) the heat exchange at the ocean surface.

2.   Sites and measurements

The major data set was obtained at the Östergarnsholm field station, situated about 4 km east of the big island Gotland in the Baltic Sea. Östergarnsholm is a very low island with no trees. At the southernmost tip of the island a 30 m tower has been erected. The distance from the tower to the shore line is between 5 and 10 m in the undisturbed sector (80°-220°). A detailed description is given in Smedman et al. (1999). A Wave rider buoy (owned and run by the Finnish Institute of Marine Research, FIMR) is moored at 36 m depth ~4 km from the tower in the direction 115°, representing the wave conditions in the upwind fetch area.

The tower was instrumented with slow-response profile temperature and wind speed at 5 heights and Solent sonic 1012R2 anemometers at three heights. This instrumentation has been employed on a semi-continuous basis since May 1995. In Högström et al., (2008a) it is demonstrated that measurements do indeed represent undisturbed marine conditions for wind from a wide sector.

During intensive measuring campaigns, we have also employed:

1. The MIUU turbulence instrument, which is a wind-vane-mounted three-component hot-film instrument with additional platinum sensors for temperature and wet-bulb temperature, which has been proven to be a precision tool (Högström and Smedman, 2004)

2. Measurements taken on the Finnish R/V Aranda cruising in the area. (Högström et al., 2008a).

3. An ASIS buoy, which is a multiple-spar buoy (Graber et al., 2000) was anchored outside Östergarnsholm during five weeks in the autumn of 2003. The instrumentation on ASIS consisted of: two sonic anemometers, air temperature, humidity and mean wind speed and direction at two levels. Figure 1 shows the Östergarnsholm site together with ASIS buoy and R/V Aranda.

Figure 1: Östergarnsholm site together with ASIS buoy and R/V Aranda

3. Analysis of wave effects

3.1. Wind speed and stress profiles

The wave field has been divided according to wave age c_p/U_8 where c_p= the peak phase speed of the waves and U_8= mean wind speed at a height of 8 m. Growing sea: $c_p/U_8<0.8$, mixed sea: $0.8< c_p/U_8<1.2$ and swell: $c_p/U>1.2$ (Only cases with wind following swell are analyzed; abs($\phi_U - \phi_{wave}$) < 90°).

The momentum flux in the MABL is characterized in Table 1 below.

Stability/wave state	Growing sea	Swell
Unstable and neutral	M-O sim. theory valid but zo is a function of cp/U	A totally different boundary layer
Stable	Low-level jets cause shear suppression	?

During swell Monin-Obukhovis similarity cannot be applied. The momentum flux in the atmospheric surface layer can be written $\tau_{tot} = \tau_{turb} + \tau_{wave} \tau_{visc}$, where the three terms on the right hand side are governed by respectively turbulence in the atmosphere, form drag created by waves and viscosity. During swell the wave induced stress is positive (directed upwards) so the total stress will be small or even positive. Figure 2a shows stress profiles during swell ($1.73< c_p/U>4.71$) from combination of data from the Östergarnsholm tower and the ASIS buoy. Figure 2b shows corresponding measurements from both aircraft and a land-based tower in the southern part of the Baltic Sea (Smedman et al., 1994).

For cases with strong swell uw is positive or close to zero but with increasing local wind speed (weaker swell) uw will become increasingly more negative. The wave induced stress will create upward transfer of momentum mediated by the pressure transport term of the TKE-budget (see below) which will result in a low-level wind maximum close to the surface. Figures 3a and b show the corresponding wind profiles.
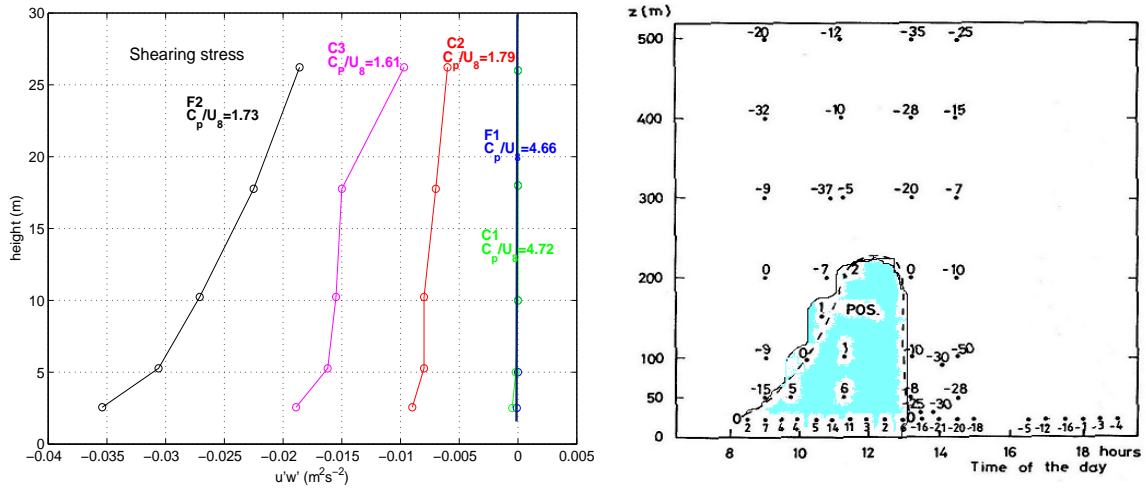
Figure 2a: Profiles of uw during 5 cases with swell. Figure 2b: Measurements of uw from aircraft and tower (lower row).
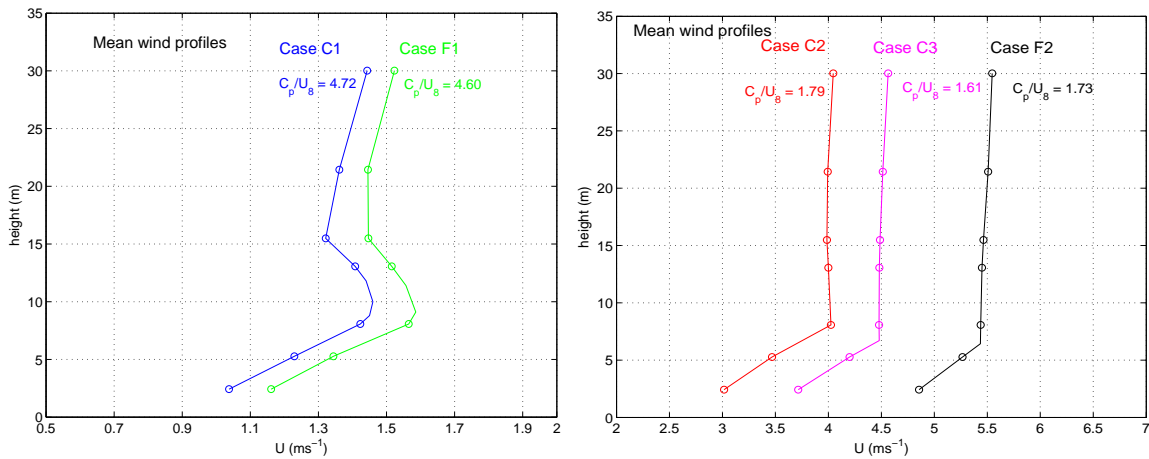

Figure 3: Wind profiles for strong swell (a) and weaker swell (b)

For a higher local wind and thus weaker swell (Figure 2b) the low-level wind maximum is transformed into a profile with a 'knee' instead. The measured wind profiles agree very well with LES simulations by Sullivan et al. (2008). Soundings through the whole boundary layer show constant wind profiles up to the top of MABL usually a couple hundred meters.

An analysis of the dimensionless wind gradient $\phi_m = \dfrac{\partial U}{\partial z} \cdot \dfrac{u_*}{kz}$ demonstrated that Monin-Obukhov theory is not valid during swell. Thus instead of a steady decrease with height from a value of unity at the surface expected for an unstable atmospheric surface layer, ϕ_m-values much in excess of unity are found for 2.56 and 5.3 m, contrasting strongly to the conditions above the maximum or the 'knee' around 10 m, where ϕ_m is close to zero. As the wind speed is constant up to the top of the atmospheric boundary layer, it is not possible to apply a top down numerical model with MO parameterization to derive the 10 m wind.

3.2. The turbulent kinetic energy budget

The turbulent kinetic energy (TKE) budget reads

$$\frac{\partial \overline{q^2}}{2\partial t} + \overline{\vec{U} \cdot \nabla(\frac{q^2}{2})} = \overline{uw}\frac{\partial \overline{U}}{\partial z} - \frac{g}{T}\overline{w\theta_v} + \frac{\partial}{\partial z}\frac{\overline{wq^2}}{2} + \frac{1}{\rho}\frac{\partial \overline{pw}}{\partial z} + \varepsilon$$

$$\quad\text{Trc}\quad\text{Adv}\qquad\text{P}\qquad\text{B}\qquad T_t\qquad T_p\qquad \varepsilon$$

The left hand side terms are found to be much smaller than the dominating terms on the right hand side, which are respectively, with colour code in Figures 4a,b: *P* (blue): shear production; *B* (red): buoyancy production; *Tt* (green): vertical divergence of turbulent transport; T_p(magenta): vertical divergence of pressure transport; and ε (black): dissipation. All terms except T_p were evaluated directly from the measurements. The remaining term, T_p is derived as a residual.

General features of the TKE-plot examples are as follows. For strong swell (4a), the pressure transport term and the dissipation are the dominant terms: The shape of the observed *Tp*-curve (full line magenta) is in agreement with theoretically expected (Högström et al., 2008b) exponential decay with height (dashed magenta curves). The weak swell case (4b) has strong mechanical production near the surface. The pressure transport term has positive sign (loss) below about 7 m, which is due to effects from surface waves of medium wavelength, having critical heights below 7 m. Above this height, *Tp* is negative (gain) and decaying with height as in Figure 4a.
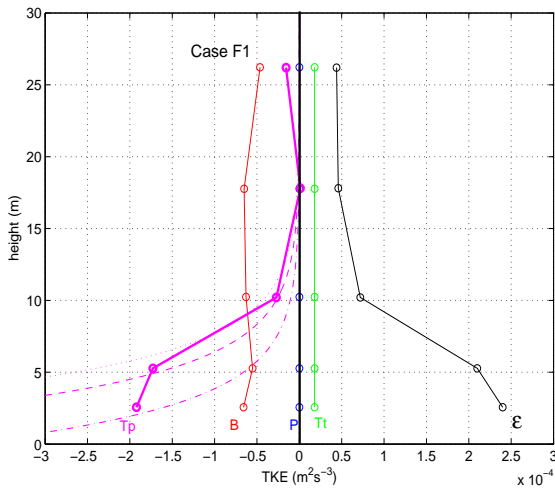

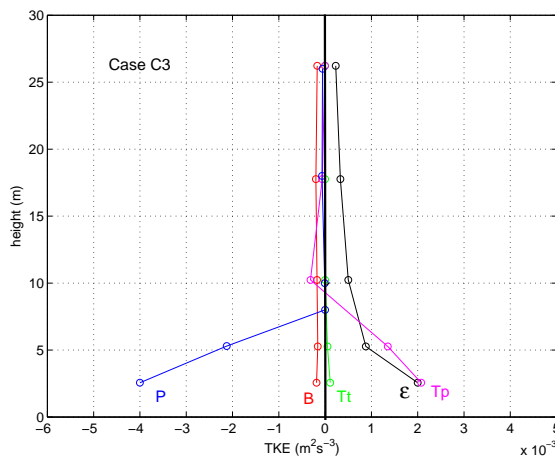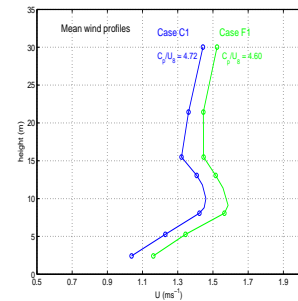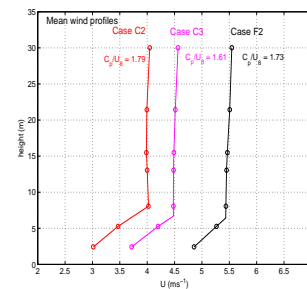*Figure 4a Example of TKE budget for strong swell.*

Figure 4b. Example of TKE budget for weak swell

3.3. Deriving a hypothetical non-swell wind profile by removing the pressure transport term

The wind profile can be expressed as $\dfrac{\partial U}{\partial z} = -\dfrac{1}{\overline{u'w'}}\left(-\dfrac{g}{T}\overline{w'\theta_v'} + \dfrac{\partial}{\partial z}\dfrac{\overline{w'q'^2}}{2} + T_p + \varepsilon\right)$

and the effect of T_p can be isolated $\left(\dfrac{\partial U}{\partial z}\right)_{Tp} = -\dfrac{T_p}{\overline{u'w'}}$ Integrating from the lowest measuring point 2.5 m to

a height z $U(z) - U(2.5m) = \displaystyle\int_{2.5m}^{z}\dfrac{T_p}{u_*^2}dz$

In Figure 5 the original, measured wind profile (blue curve) and the corresponding wind profile obtained after subtracting the contribution from Tp (red curve) is shown for one case. It is clear that the pressure transport term causes the 'knee' feature in the swell wind profile.
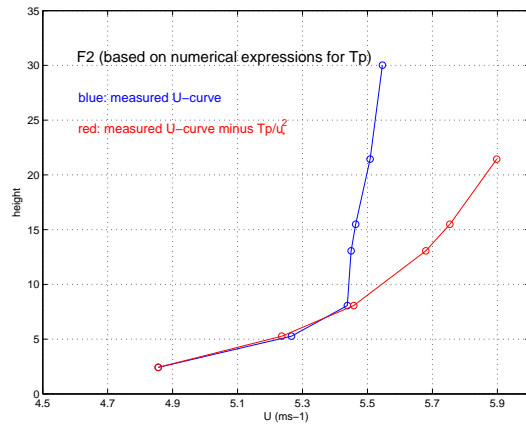

Figure 5: Reconstruction of wind profile.

4. Analysis of the sensible and latent heat exchange at the ocean surface

In models all turbulent fluxes must be expressed as functions of mean variables. The bulk exchange coefficient for the sensible heat flux C_H is defined: $C_H = \overline{w'\theta'}/(U_{10} - U_s)(\Theta_w - \Theta_{10})$ where $\overline{w'\theta'}$ = the kinematic heat flux at the surface, U_{10} = mean wind speed at 10m, U_s = mean wind speed at the water surface, Θ_w = potential temperature of the water surface and Θ_{10} = potential temperature at 10 m. C_E for latent heat can be defined in a similar way.

For unstable stratification C_H can be reduced to neutral stratification $C_{HN} = \dfrac{\kappa^2}{\{\ln(z/z_0)\}\{\ln(z/z_{0T})\}}$ where

z_o and z_{ot} are the roughness lengths for wind and temperature respectively. In a similar way C_{EN} is defined.

4.1. The UVCN turbulence regime

It is well established from experimental and theoretical studies that for slightly unstable atmospheric boundary layers longitudinal roll structures that extend vertically throughout the entire boundary layer dominate. The longitudinal roll model does, however, not explain the transition of the temperature spectra that we observe for the combination of relatively strong wind ($U_{10} > c.10$ ms[-1]) and small air-sea temperature difference (0.5-1.5K), the Unstable Very Close to Neutral regime, UVCN, Figure 6.
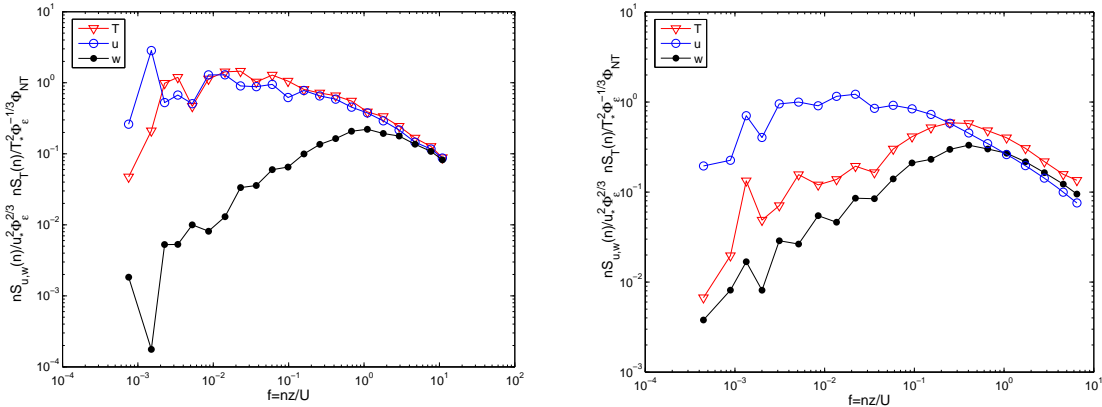
Figure 6a. Example of u, w and temperature spectra for unstable stratification (L=-14) and in Figure 6 b corresponding spectra for UVCN regime (L=-385).

During unstable stratification the temperature spectra resemble the spectra of the longitudinal wind component but in the UVCN regime the shape of temperature spectra is similar to the w-spectra. This can also be seen in the $w\theta$ co-spectra (Figure 7). For unstable stratification the peak frequency of the co-spectrum is around $5 \cdot 10^{-2}$ but with decreasing stability the peak frequency is moving towards much higher frequencies. The observed features are interpreted (Smedman et al., 2007a) as possible manifestations of a bifurcation of the large scale eddy structure towards a state in which there are quasi-steady longitudinal rolls and, on a smaller scale, unsteady detached eddies. Our interpretation of the results from the measurements is that, in the UVCN regime, the latter component plays a significant role for the exchange of sensible heat. Thus, high-speed air from above the surface layer is engulfed into the surface layer and brought down to the surface as detached eddies.
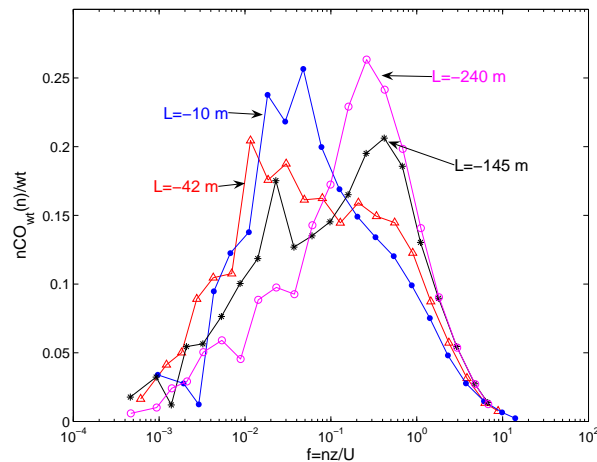

Figure 7: Normalized co-spectra of heat flux for different stabilities.

4.2. The exchange coefficients C_{HN} and C_{EN}

The relative increase in heat flux in the UVCN regime is bound to show up in the bulk parameters, C_{HN} and C_{EN} and we now set the limit for the UNCN regime as follows: air-water temperature difference $\Delta T < 3^{o}$ and wind speed $U > 10$ ms^{-1}. In Figure 8a the Stanton number for sensible heat (C_{HN}) is plotted as a function of wind speed. The red and blue dots represent measurements with the MIUU hot- wire instrument and temperature measured with a platinum sensor, blue dots for $\Delta T > 3^{o}$ and red dots for $\Delta T < 2^{o}$. Mean sonic values are given in black. For $U < 10$ ms^{-1} there is not much variation in the mean between the instruments but for

higher wind speeds the MIUU data are systematically higher. The deviation between the data sets is largest for measurements with $\Delta T < 2^o$, indicated with red dots in Figure 8a.
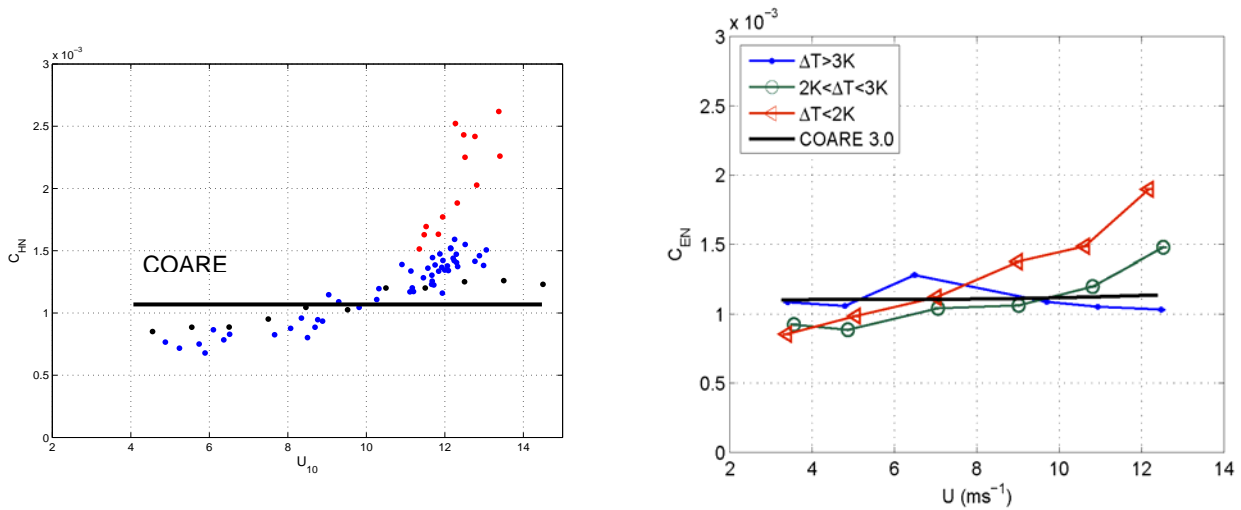

Figure 8 shows C_{HN} (a) and C_{EN} (b) as function of U. In Figure 8a blue and red dots represent MIUU data and black dote sonic data. The humidity flux in Figure 8b is measured with LICOR and sonic instruments.

The reason for this can be found in the temperature spectra and corresponding heat flux co-spectra. Figure 9 compares mean normalized $w\theta$ co-spectra for two groups of data: a) $U < 7$ ms^{-1} and $\Delta T > 3^o$ and b) $U > 10$ ms^{-1} and $\Delta T < 2^o$ measured with the MIUU instrument (o) and sonic (•). Good agreement is obtained for case a) but gross disagreement for case b). It is obvious that the sonic instrument misses much of the co-spectral energy at relatively high frequencies and hence the recorded flux is underestimated (Smedman et al., 2007b).
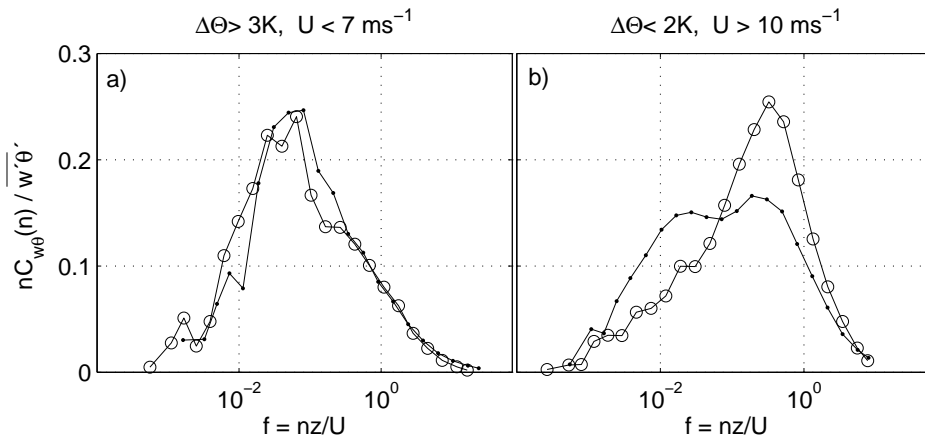

Figure 9. Heat fluxes measured with Sonic and the MIUU instrument.

Figure 8b shows C_{EN} as a function of wind speed where humidity is measured with LICOR and the vertical wind speed with sonic. For $U < 8$ ms^{-1} all three curves agree with the COARE algorithm (black solid line) but for $U > 8$ and $\Delta T < 3^o$ (the UVCN regime) the measured Dalton number is much higher (Sahlee et al., 2008).

The analysis so far only includes data from Östergarnsholm and more data are needed to show the generality of the UVCN regime. However, it is difficult to find suitable data because temperature is almost always measured with a sonic and in addition in most published data set measurements with $\Delta T < 2-3^o$ are removed. Data from an experiment (Agile) in Lake Ontario 1994-95 where temperature also was measured with thermocouple have been put to out disposal by W. Drennan (Donelan and Drennan, 1995). The analysis shows general agreement with our data. In Figure 10a C_{HN} is plotted as a function of U and the solid curves

(blue= sonic, red= thermocouple) represent mean values for $\Delta T > 3^{o}$. The red and blue dots show individual values with small ΔT, actual values of wich are written in the plot. Data with the corresponding plot for C_{EN} is given in Figure 10b. The solid curves are the same as in Figure 8b (Östergarnsholm data) and the red dots individual values from the Agile experiment measured with Licor and with ΔT indicated for each measurement.
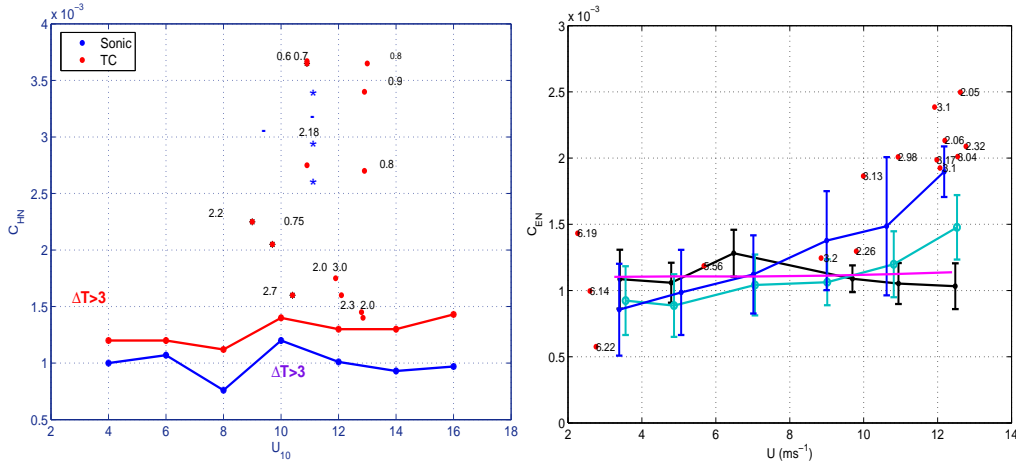

Figure 10 Data from the Agile experiment showing C_{HN} (10a) and C_{EN}(10b). See text for explanation.

Both the Stanton and Dalton coefficients increase for high wind speed and small temperature differences. The difference in co-spectral shape between measurements of sonic temperature and thermocouple is very similar to what we find from the Östergarnsholm site (Figure 11)
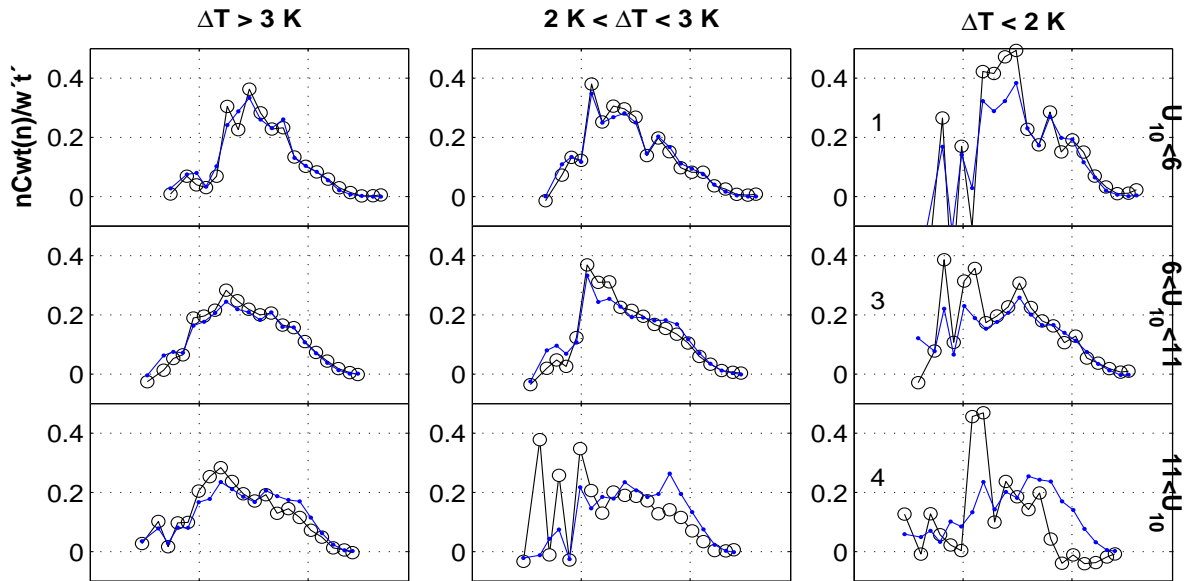

Figure 11 Normalized heat fluxes measured with sonic (O) and thermocouple (•) for different ΔT and wind speed.

To investigate the effect of the UVCN regime on a global scale ERA-40 reanalyses data have been used. In Figure 12a relative frequency of the occurrence of UVCN conditions is shown. High probability is found over Southern Oceans where the wind speed is high but also in the Northern Atlantic and Pacific and in monsoon areas. Figure 12b gives the differences in latent heat fluxes between standard parameterization and the UVCN algorithm. Again the differences are largest in areas where high winds are common (Sahlee et al., 2008).
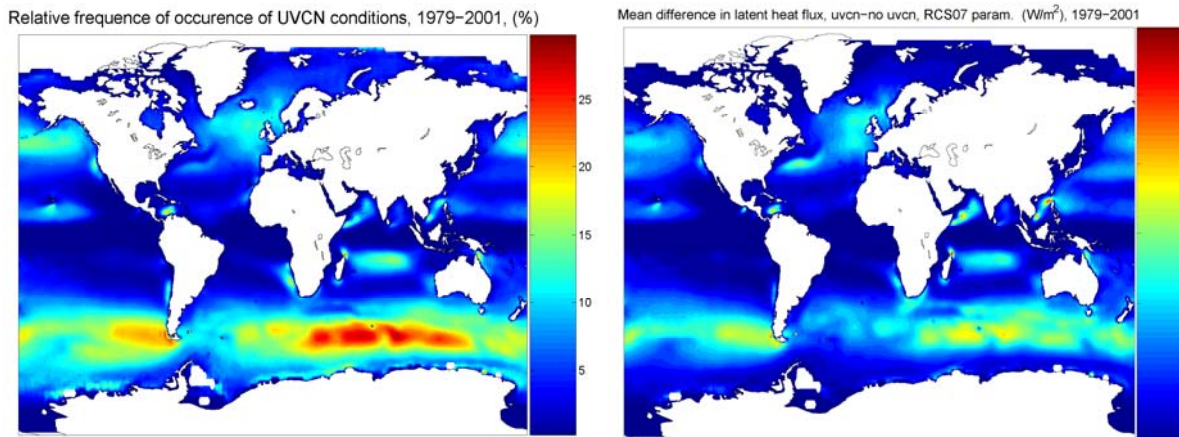

Figure 12 Differences in latent heat flux calculated with COARE and the UVCN algorithms.

5.   Conclusions

From our analysis it is clear that exchange processes at the ocean surface will influence the structure of the MABL, but at the same time may dynamical processes in the atmosphere affect the transfer at the surface,

1. When the wind speed is increasing waves are increasing and thus also the roughness length. Changing the roughness length will influence Φ_m in the MABL but only close to the surface. During growing sea the critical height (or the wave boundary layer height) is less than 1 m and the profile of the TKE budget is similar to what is found over land.

2. During swell the form drag at the ocean surface produces an up-ward momentum flux which in turn creates a totally different MABL. The whole boundary layer is affected and can be characterized as: i) low-level jet at very low heights, ii) constant wind speed above the jet which influences Φ_m in the whole MABL, iii) momentum flux is small or even positive, iv) M-O similarity is not valid, v) spectra resemble free convection spectra and v) the pressure transport term is an important part of the TKE budget.

3. The dynamics of the MABL influences the exchange of sensible and latent heat at the ocean surface. When the convective boundary layer is ruled by horizontal rolls the well known COARE algorithm is valid. But when detached eddied originating from the upper part of the surface layer is present (UVCN regime) the heat fluxes are increased and the Φ_h-function goes to zero. It is important to point out that this will only be seen in the lower part of the boundary layer. The following explains why the UVCN regime has not been observed earlier: i) sonic temperature fail to measure temperature fluctuations correctly when σ_T is small (high wind speed, small ΔT), ii) data with small ΔT are often removed and iii) measurements are taken at heights above the UVCN layer.

During stable stratification (not discussed previous in the main text) the influence of waves is small and can be neglected but stability will decrease the exchange coefficients. If a low-level jet is present the increased shear below the jet may cause substantial suppression of the heat flux.

6.   References

Donelan, M. A. and W. M. Drennan, 1995: Direct field measurements of the flux of carbon dioxide. *Air-Water Gas Transfer*, Aeon-Verlag, 677-683.

Graber, H.C., E.A. Terray, M.A. Donelan, W.M. Drennan, J.C. Van Leer and D.B. Peters, 2000: ASIS – a new air-sea interaction spar buoy: design and performance at sea. *J. Atmos. Oceanic Technol.* **17**, 708-720.

Högström, U. and A. Smedman, 2004: Accuracy of sonic anemometers: Laminar wind-tunnel calibrations compared to atmospheric in situ calibrations against a reference instrument. *Bound.-Layer Meteorol*. **111(1),** 33-54.

Högström, U., E. Sahlée, W.M. Drennan, K.K. Kahma, A.-S. Smedman, C. Johansson, H. Pettersson, A. Rutgersson, L. Tuomi, F. Zhang and M. Johansson, 2008a**:** To what extent can we believe measurements on a land-based tower to represent upwind open sea conditions? Accepted for publication in *Boreal Environment Res,*.

Högström, U., A. Smedman, E. Sahlée, W.M. Drennan, K.K. Kahma, H. Pettersson, F. Zhang, 2008b: The atmospheric boundary layer during swell – a field study of the governing mechanism. *Submitted to Journal of Atmospheric Sciences.*

Sahlee**,** E and A. Smedman, U. Högström and A. Rutgersson, 2008: Re-evaluation of the bulk exchange coefficient for humidity at sea during unstable and neutral conditions, *J. Phys. Ocean*., **38 (1),** 257-272

Sahlée E., Smedman A., Högström U., 2008: Influence of a new turbulent regime on the global air-sea heat fluxes, J. Climate, 21, 5925-5941

Smedman, A-S., M. Tjernström and U. Högström, 1994: The near-neutral marine atmospheric boundary layer with no shearing stress: A case study. *J. Atm. Sci.*, **51**, 3399-3411. Smedman,

Smedman A.., U. Högström, H. Bergström, A. Rutgersson, K.K. Kahma and H. Pettersson, 1999: A case study of air-sea interaction during swell conditions. *J. Geophys. Res.,***104**, 25,833-25,851.

Smedman, A., U. Högström, J.C.R. Hunt and E. Sahlée, 2007a: The changing eddy structure near the surface in unstable close to neutral atmospheric boundary layers and the effects on heat/mass transfer, especially over the ocean. *Quart. J. Roy. Meteorol. Soc.,***133**, 37-51..

Smedman, A., U. Högström, E. Sahlée, and C. Johasson, 2007b: Critical re-evaluation of the bulk transfer coefficient for sensible heat over the ocean during unstable and neutral conditions. *Quart. J. Roy. Meteorol. Soc.,***133**, 227-250.

Smedman, A., Högström, U., E. Sahlée, W.M. Drennan, K.K. Kahma, H. Pettersson, F. Zhang, 2008: Observational study of marine atmospheric boundary layer Characteristics during swell. *Submitted to Journal of Atmospheric Sciences.*

Sullivan, P.P., J.B. Edson, T. Hristov and J.C. Mc Williams, 2008: Large eddy simulationsand observations of atmospheric marine boundary layers above non-equilibrium surface waves. *J. Atm. Sci.,* 65, 1225-1245.